

Densification of porous bodies in a granular pressure-transmitting medium

E.A. Olevsky^{a,*}, J. Ma^a, J.C. LaSalvia^b, M.A. Meyers^c

^a San Diego State University, Mechanical Engineering Department, 5500 Campanile Drive, San Diego, CA 92182-1323, USA

^b Materials Division, US Army Research Laboratory, APG, MD 21005-5069, USA

^c Department of Mechanical and Aerospace Engineering, University of California, San Diego, La Jolla, CA 92093-0416, USA

Received 5 July 2006; accepted 25 September 2006

Available online 11 December 2006

Abstract

Densification is a critical step in the manufacture of near-net-shaped components via powder processing. A non-isostatic stress state will in general result in shape distortion in addition to densification. In the quasi-isostatic pressing (QIP) process the green body is placed into a granular pressure-transmitting medium (i.e. PTM), which is itself contained in a rigid die. Upon the application of a uniaxial load, the PTM redistributes the tractions on the green body, thereby creating a stress state that is quasi-isostatic. The character of the deformation of the PTM is studied using model experiments on pressing of the PTM in a rigid die and a scanning electron microscopy analysis of the PTM powder. An important problem of the optimization of the PTM chemical composition enabling the maximum densification of a porous specimen with the minimum possible shape distortion is solved. The results of modeling agree satisfactorily with the experimental data on cold QIPing Ti and Ni powder samples and hot QIPing TiC–TiNi cermet composites.

© 2006 Acta Materialia Inc. Published by Elsevier Ltd. All rights reserved.

Keywords: Quasi-isostatic pressing; Shape change; Deformation of porous bodies; Self-propagating high-temperature synthesis

1. Introduction

Densification of porous materials by the application of compressive stress is an important mechanical processing method. Porous bodies undergo volume change in addition to shape change during mechanical treatment; this introduces additional considerations with regard to possible deformation modes, in comparison to fully dense bodies.

Several methods are used to insure densification of porous materials (for more details, see German [1]). The principal ones are shown in Fig. 1. Stress states imposed by the different methods depend on the loading mode.

In the terminology of mechanical treatment of porous bodies, the volume change relative to the shape change corresponds to the “stiffness” of the deformation modes. Free

up-setting has the lowest stiffness of the deformation modes shown in Fig. 1. Isostatic pressing has the highest stiffness. It is evident that the higher stiffness causes the larger densification degree, which is of significant importance for final mechanical properties. In this regard, isostatic pressing has the highest potential for the production of full-dense articles. However, the high cost of equipment associated with isostatic pressing (e.g. CIP and HIP) of particulate and porous bodies lends impetus for other cost-effective technologies, which are technically simple while providing a sufficiently high degree of stiffness with respect to the deformation mode.

Uniaxial pressing with a pressure-transmitting medium (PTM) (Fig. 1) has been attracting attention as one such possible alternative method. Known as the Ceracon [2–4] or quasi-isostatic pressing (QIP) process, it has been utilized industrially in manufacturing [1,5,6] and, in particular, in combination with self-propagating high-temperature synthesis (SHS) [7–20]. This technological

* Corresponding author. Tel.: +1 619 5946329; fax: +1 619 5943599.
E-mail address: eolevsky@mail.sdsu.edu (E.A. Olevsky).

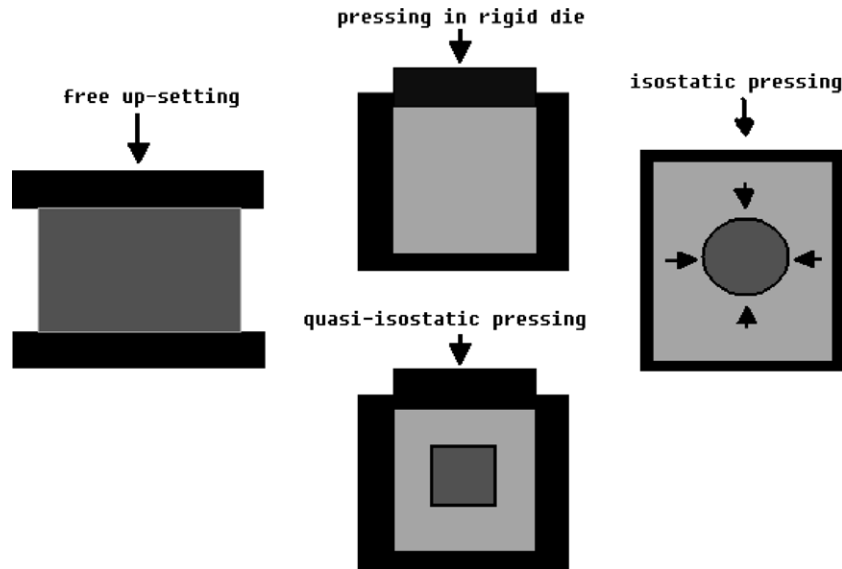


Fig. 1. Deformation schematics for different pressure densification processes.

sequence was pioneered by Merzhanov and co-workers [21] in Russia and implemented in the US by Raman et al. [2]. When combined with SHS, QIP offers a relatively simple processing method by which hundreds of industrially useful materials can be produced and shaped into engineering components [3]. A granular PTM (alumina or alumina with graphite powder) serves not only as a load transmitter, but also as a natural thermal insulator which prevents substantial heat loss and minimizes temperature gradients during SHS. This leads to increased flexibility in the pressurization cycle, as well as microstructural uniformity (grain size, phase distribution, etc.).

In contrast to a conventional containerless isostatic pressing, a considerable shape change is obtained under QIP [1,4].

In light of the development of near-net-shape technologies, the analysis of both shape and volume changes under QIP is of considerable importance. The factors which influence the shape and the volume change of a porous body include the initial porosities of both the PTM and the porous body, and their respective constitutive properties. The objective of the present work is the investigation of the effect of these factors on shape change during QIP.

The paper is organized as follows: Section 2 provides a description of a constitutive model for nonlinear-viscous deformation of porous bodies. Section 3 comprises the theoretical analysis of the quasi-isostatic pressing. In this section, the change in the aspect ratio for a cylindrical porous body is analyzed for the conditions of free up-setting, pressing in a rigid die, isostatic pressing and QIP. Section 4 includes the experimental data on the constitutive behavior of PTM. Section 5 includes the solution of an important problem of the optimization of the PTM chemical composition (the concentrations of graphite and alumina powders) enabling maximum densification with minimum

possible shape distortion. Section 6 presents the results of cold QIP experiments on Ti and Ni porous bodies and hot QIP experiments on TiC–TiNi cermet composites. A comparison of experimental and theoretical results is given in Section 7.

2. Theory of nonlinear-viscous deformation of porous bodies

The mechanical response of a nonlinear-viscous porous body to an externally applied pressure (which is significantly higher than the sintering-imposed stresses) can be described [22–26] by a rheological (constitutive) relationship of a continuum theory of sintering connecting components of the stress tensor σ_{ij} and the strain rate tensor $\dot{\epsilon}_{ij}$ and omitting the effective sintering stress:

$$\sigma_{ij} = \frac{\sigma(W)}{W} \left[\varphi \dot{\epsilon}_{ij} + \left(\psi - \frac{1}{3} \varphi \right) \dot{\epsilon} \delta_{ij} \right] \quad (1)$$

where W is the so-called equivalent strain rate, and $\sigma(W)$ is the equivalent stress, φ and ψ are the shear and bulk viscosity moduli, which depend on porosity θ , δ_{ij} is a Kronecker symbol ($\delta_{ij} = 1$ if $i = j$ and $\delta_{ij} = 0$ if $i \neq j$) and $\dot{\epsilon}$ is the first invariant of the strain rate tensor, i.e. the sum of the tensor diagonal components: $\dot{\epsilon} = \dot{\epsilon}_{11} + \dot{\epsilon}_{22} + \dot{\epsilon}_{33}$.

The porosity θ is defined as $1 - \frac{\rho}{\rho_T}$, where ρ and ρ_T relative and theoretical (corresponding to a fully dense state) densities, respectively. Physically, $\dot{\epsilon}$ represents the volume change rate of a porous body.

Equivalent strain rate W is connected with the current porosity and with the invariants of the strain rate tensor:

$$W = \frac{1}{\sqrt{1-\theta}} \sqrt{\varphi \dot{\gamma}^2 + \psi \dot{\epsilon}^2} \quad (2)$$

(the origin of this equation is explained in Ref. [24]); $\dot{\gamma}$ is the second invariant of the strain rate tensor deviator and represents, physically, the shape change rate of a porous body:

$$\dot{\gamma} = \left[\left(\dot{\epsilon}_{ij} - \frac{1}{3} \dot{\epsilon} \delta_{ij} \right) \left(\dot{\epsilon}_{ij} - \frac{1}{3} \dot{\epsilon} \delta_{ij} \right) \right]^{\frac{1}{2}} \quad (3)$$

Parameter $\sigma(W)$ determines the constitutive behavior of a porous material. If $\sigma(W)$ is described by the linear relationship $\sigma(W) = 2\eta_0 W$, where η_0 is the shear viscosity of a fully dense material, one obtains the equation corresponding to the behavior of a linear-viscous porous body (used to describe hot deformation of amorphous materials):

$$\sigma_{ij} = 2\eta_0 \left[\varphi \dot{\epsilon}_{ij} + \left(\psi - \frac{1}{3} \varphi \right) \dot{\epsilon} \delta_{ij} \right] \quad (4)$$

If $\sigma(W)$ is a constant ($\sigma(W) = \sigma_y$, σ_y being the yield stress for a fully dense material), the equation corresponding to a rigid-plastic porous body (used to describe cold deformation processing) is obtained:

$$\sigma_{ij} = \frac{\sigma_y \sqrt{1-\theta}}{\sqrt{\varphi \dot{\gamma}^2 + \psi \dot{\epsilon}^2}} \left[\varphi \dot{\epsilon}_{ij} + \left(\psi - \frac{1}{3} \varphi \right) \dot{\epsilon} \delta_{ij} \right] \quad (5)$$

In the general case, $\sigma(W)$ is described by a nonlinear relationship. For example, for hot deformation of crystal-line materials, a power law is used [1] ($\sigma(W) = AW^m$ where A and m are the material constants, $0 \leq m \leq 1$). In this case, we have:

$$\sigma_{ij} = A \left(\frac{\sqrt{\varphi \dot{\gamma}^2 + \psi \dot{\epsilon}^2}}{\sqrt{1-\theta}} \right)^{m-1} \left[\varphi \dot{\epsilon}_{ij} + \left(\psi - \frac{1}{3} \varphi \right) \dot{\epsilon} \delta_{ij} \right] \quad (6)$$

It can be noted, that, for $m = 1$, Eq. (6) is transformed into Eq. (4) ($A = 2\eta_0$) and, for $m = 0$, Eq. (6) is transformed into Eq. (5) ($A = \sigma_y$).

Thus, linear-viscous and rigid-plastic behaviors are two limiting cases for a nonlinear-viscous constitutive behavior.

3. Analysis of the densification processes

Based on the theory of nonlinear-viscous deformation of porous bodies described in the previous section, it is possible to assess both the densification kinetics and the shape evolution of a specimen subjected to QIP.

It is assumed that the stresses are uniform within both the PTM and the porous body. For simplicity, a cylindrical geometry is assumed and a cylindrical coordinate system is used.

The volume-change rate $\dot{\epsilon}$ and the shape-change rate $\dot{\gamma}$ are given by:

$$\dot{\epsilon} = \dot{\epsilon}_{zz} + 2\dot{\epsilon}_{rr} = \left[1 + 2 \left(\frac{\dot{\epsilon}_{rr}}{\dot{\epsilon}_{zz}} \right) \right] \dot{\epsilon}_{zz} = \frac{\dot{\theta}}{1-\theta} \quad (7)$$

$$\dot{\gamma} = \sqrt{\frac{2}{3}} |\dot{\epsilon}_{zz} - \dot{\epsilon}_{rr}| = \sqrt{\frac{2}{3}} \left| 1 - \left(\frac{\dot{\epsilon}_{rr}}{\dot{\epsilon}_{zz}} \right) \right| |\dot{\epsilon}_{zz}| \quad (8)$$

where $\dot{\epsilon}_{zz}$, $\dot{\epsilon}_{rr}$ and θ are the axial strain rate, radial strain rate and porosity, respectively. For a cylindrical specimen, the axial and radial strain rates are given by (see Fig. 2):

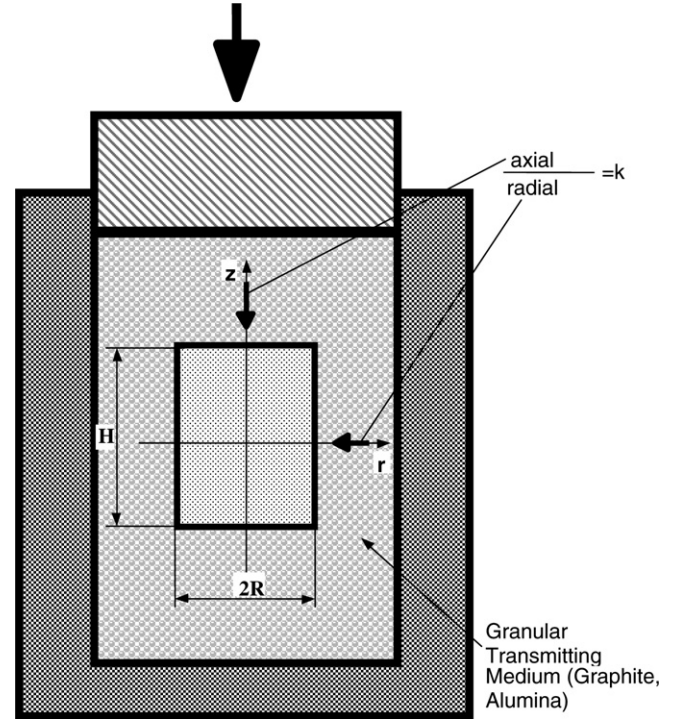


Fig. 2. Conditions of biaxial loading of a porous sample during QIP.

$$\dot{\epsilon}_{zz} = \frac{\dot{H}}{H_0}; \quad \dot{\epsilon}_{rr} = \frac{\dot{R}}{R_0} \quad (9)$$

where H and R are the instantaneous cylinder height and radius. Substituting Eq. (3) into Eq. (8) gives the following relationship for the shape-change rate:

$$\dot{\gamma} = \sqrt{\frac{2}{3}} \left| \frac{\dot{H}}{H} - \frac{\dot{R}}{R} \right| \quad (10)$$

This expression will be used to derive relationships between the height and the radius of the cylindrical specimen and the porosity.

The radial σ_{rr} and the axial σ_{zz} stresses can be written as (see Eqs. (1) and (6)):

$$\sigma_{rr} = AW^{m-1} \varphi \left\{ \left(\frac{\dot{\epsilon}_{rr}}{\dot{\epsilon}_{zz}} \right) - \frac{1}{3} \left[1 - 3 \left(\frac{\psi}{\varphi} \right) \right] \left[1 + 2 \left(\frac{\dot{\epsilon}_{rr}}{\dot{\epsilon}_{zz}} \right) \right] \right\} \dot{\epsilon}_{zz} \quad (11)$$

$$\sigma_{zz} = AW^{m-1} \varphi \left\{ 1 - \frac{1}{3} \left[1 - 3 \left(\frac{\psi}{\varphi} \right) \right] \left[1 + 2 \left(\frac{\dot{\epsilon}_{rr}}{\dot{\epsilon}_{zz}} \right) \right] \right\} \dot{\epsilon}_{zz} \quad (12)$$

where W is the equivalent strain rate, A and m ($0 \leq m \leq 1$) are material constants, and φ and ψ are the normalized shear and bulk viscosity moduli (see Section 2). The shear and bulk viscosity moduli depend upon porosity θ and are given by [22–26]:

$$\varphi = (1-\theta)^2 \quad (13)$$

$$\psi = \frac{2}{3} \frac{(1-\theta)^3}{\theta} \quad (14)$$

From Eqs. (13) and (14), the ratio of the bulk to shear viscosity moduli is obtained:

$$\frac{\psi}{\varphi} = \frac{2}{3} \left(\frac{1-\theta}{\theta} \right) \quad (15)$$

The equivalent strain rate W is defined, by substituting Eqs. (7), (8) and (13) into Eq. (2), as:

$$W = \left\{ \frac{\varphi}{1-\theta} \left[\dot{\gamma}^2 + \left(\frac{\psi}{\varphi} \right) \dot{\epsilon}^2 \right] \right\}^{\frac{1}{2}} \\ = \left[(1-\theta) \left\{ \frac{2}{3} \left[1 - \left(\frac{\dot{\epsilon}_{rr}}{\dot{\epsilon}_{zz}} \right) \right]^2 + \left(\frac{\psi}{\varphi} \right) \left[1 + 2 \left(\frac{\dot{\epsilon}_{rr}}{\dot{\epsilon}_{zz}} \right) \right]^2 \right\} \right]^{\frac{1}{2}} |\dot{\epsilon}_{zz}| \quad (16)$$

If the specimen's volume is much smaller than the volume of the PTM-containing rigid die, then the specimen's deformation is accompanied by a negligible deformation of the PTM material. Hence, the granular flow of PTM is minimal and it can be assumed that the PTM (i.e. PTM) behaves as a purely elastic porous body (see Section 4 and Appendix). It is further assumed that the presence of the porous cylindrical body within the PTM provides a negligible effect on its state-of-stress as a result of the applied axial load. This is equivalent to imagining the porous cylindrical body embedded in an infinitely extended PTM with a far-field applied stress σ_{zz}^{∞} at its boundary. The PTM itself is assumed to be under the condition of a uniaxial load with a lateral confinement (i.e. pressing in a rigid die). Therefore, the sample can be considered under conditions of biaxial loading (Fig. 2).

For the PTM, the axial and radial stresses are related to the axial strain ϵ_{zz} by the Hooke's law and are given by (see Eq. (A1) in Appendix):

$$\sigma_{zz} = \left[\frac{1-\nu}{(1+\nu)(1-2\nu)} \right] E \epsilon_{zz} \quad (17)$$

$$\sigma_{rr} = \left[\frac{\nu}{(1+\nu)(1-2\nu)} \right] E \epsilon_{zz} \quad (18)$$

where ν and E are the Poisson's ratio and Young's modulus for the PTM, respectively. These depend upon the PTM porosity θ_p and are given by (see Section 4 and Appendix):

$$\nu = \frac{2-3\theta_p}{4-3\theta_p} \quad (19)$$

$$E(C, \theta_p) = 384.55(C+1)^{-0.22475} (0.0188(1-\theta_p) - 0.8764) \quad (20)$$

where C is the concentration of graphite in the PTM. The ratio of the axial stress to the radial stress is therefore given by:

$$\frac{\sigma_{zz}}{\sigma_{rr}} = \frac{1-\nu}{\nu} = \frac{2}{2-3\theta_p} = k \quad (21)$$

The ratio of the radial stress to the axial stress is also obtained from Eqs. (11) and (12) And it is given by:

$$\frac{\sigma_{rr}}{\sigma_{zz}} = \frac{\left(\frac{\dot{\epsilon}_{rr}}{\dot{\epsilon}_{zz}} \right) - \frac{1}{3} \left[1 - 3 \left(\frac{\psi}{\varphi} \right) \right] \left[1 + 2 \left(\frac{\dot{\epsilon}_{rr}}{\dot{\epsilon}_{zz}} \right) \right]}{1 - \frac{1}{3} \left[1 - 3 \left(\frac{\psi}{\varphi} \right) \right] \left[1 + 2 \left(\frac{\dot{\epsilon}_{rr}}{\dot{\epsilon}_{zz}} \right) \right]} \quad (22)$$

By substituting Eq. (15) into Eqs. (21) and (22), the following expression for the axial/radial strain rate ratio is obtained:

$$\frac{\dot{\epsilon}_{rr}}{\dot{\epsilon}_{zz}} = \frac{\theta - \theta_p}{2\theta_p + (1-3\theta_p)\theta} \quad (23)$$

It is methodologically useful to compare Eq. (23) with the following expressions for axial/radial strain rate ratio in conventional densification processes [28]:

$$\frac{\dot{\epsilon}_{rr}}{\dot{\epsilon}_{zz}} = \frac{1-3\left(\frac{\psi}{\varphi}\right)}{1+6\left(\frac{\psi}{\varphi}\right)} = -\left(\frac{2-3\theta}{4-3\theta}\right) \text{ for free up-setting (pressing} \\ \text{without lateral confinement, } \sigma_{rr} = 0) \quad (24)$$

$$\frac{\dot{\epsilon}_{rr}}{\dot{\epsilon}_{zz}} = 0 \text{ for pressing in a rigid die (pressing with lateral} \\ \text{confinement, } \dot{\epsilon}_{rr} = 0) \quad (25)$$

$$\frac{\dot{\epsilon}_{rr}}{\dot{\epsilon}_{zz}} = 1 \text{ for isostatic pressing } (\dot{\epsilon}_{rr} = \dot{\epsilon}_{zz} \Rightarrow \dot{\epsilon} = 3\dot{\epsilon}_{zz}; \dot{\gamma} = 0) \quad (26)$$

If $k = \frac{2}{2-3\theta}$ (which means that $\theta = \theta_p$), then $\dot{\epsilon}_{rr} = 0$, and one has conditions of pressing in a rigid die. If $k = 1$ (i.e. if $\theta_p = 0$, which means that PTM is an incompressible material), $\dot{\epsilon}_{rr} = \dot{\epsilon}_{zz}$, and the conditions of isostatic pressing are achieved.

If $k \rightarrow \infty$ (i.e. if $\theta_p = 2/3$), which approximately corresponds to the density of packed isomeric spherical particles, then $\dot{\epsilon}_{rr} = \frac{3\theta-2}{4-3\theta} \dot{\epsilon}_{zz}$, and one has the conditions of free up-setting (see Eq. (24)).

In Fig. 3, the curves corresponding to the relationships between the radial/axial strain rate ratio and sample's porosity (in accordance with Eq. (23)) for various PTM porosities are shown. For comparison, the curves corresponding to the conditions of free up-setting (Eq. (24)), pressing in a rigid die ($\frac{\dot{\epsilon}_{rr}}{\dot{\epsilon}_{zz}} = 0$) and isostatic pressing ($\frac{\dot{\epsilon}_{rr}}{\dot{\epsilon}_{zz}} = 1$) are also shown.

The data in Fig. 3 indicate that, for high PTM porosities, the porous material deformation mode under QIP can be closer to the conditions of free-upsetting rather than to the isostatic pressing ones.

Mostly, the radial/axial strain rate ratio, for $\theta_p > 0.5$, is in between the curves corresponding to pressing in a rigid die and free up-setting. This fact testifies the intensive shape change under QIP which is the distinctive feature of this process in comparison with the conventional containerless isostatic pressing.

For QIP, the equivalent strain rate is given by:

$$W = \sqrt{6} \left[\frac{(1-\theta_p)(1-\theta)^{\frac{2}{3}}}{2\theta_p + (1-3\theta_p)\theta} \right] \left[\left(\frac{\theta_p}{1-\theta_p} \right)^2 + \frac{\theta}{1-\theta} \right]^{\frac{1}{2}} |\dot{\epsilon}_{zz}| \quad (27)$$

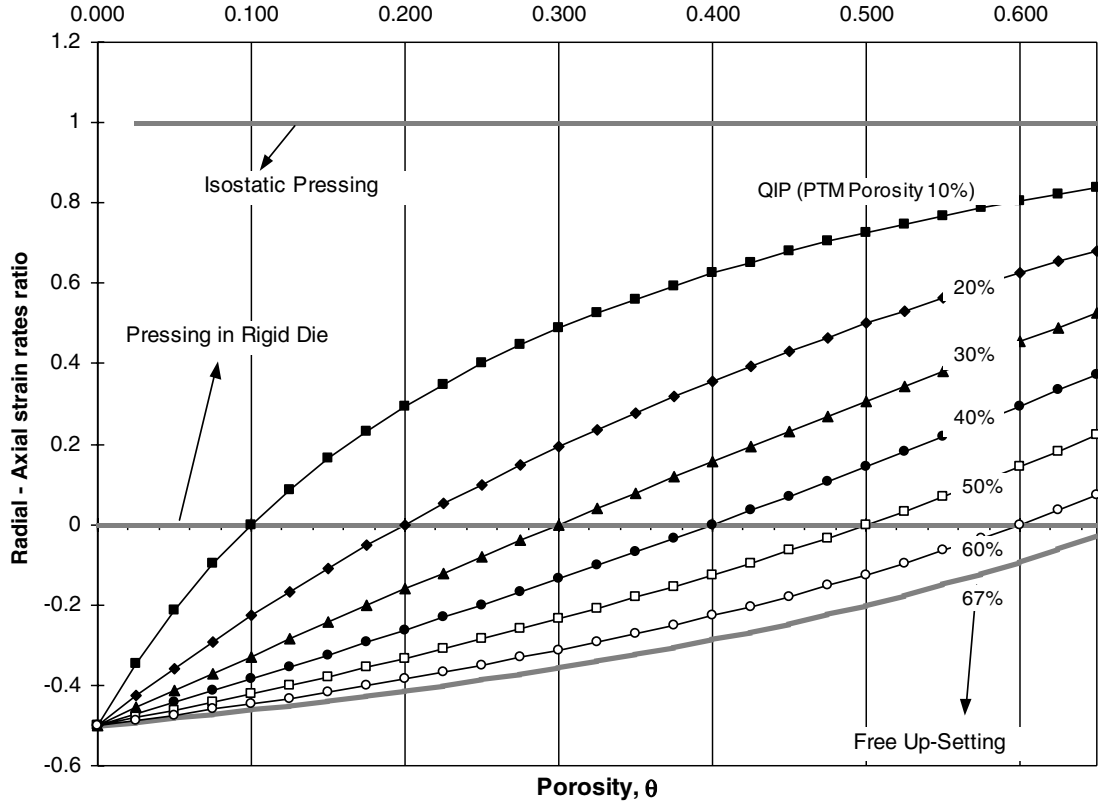


Fig. 3. Radial-axial strain rate ratio vs. porosity for different processes of treatment by pressure.

The axial stress is therefore given by:

$$\sigma_{zz} = -A \left(\frac{2^{m+1}}{3^{1-m}} \right)^{\frac{1}{2}} \left[\frac{(1 - \theta_p)^{m-1} (1 - \theta)^{\frac{3}{2}(m+1)}}{[2\theta_p + \theta(1 - 3\theta_p)]^m} \right] \times \left[\left(\frac{\theta_p}{1 - \theta_p} \right)^2 + \frac{\theta}{1 + \theta} \right]^{\frac{m-1}{2}} |\dot{\epsilon}_{zz}|^m \quad (28)$$

The axial strain rate is obtained by rearranging Eq. (28):

$$|\dot{\epsilon}_{zz}| = \left(\frac{3^{1-m}}{2^{m+1}} \right)^{\frac{1}{2m}} \left[\frac{2\theta_p + \theta(1 - 3\theta_p)}{(1 - \theta_p)^{\frac{m-1}{m}} (1 - \theta)^{\frac{3(m+1)}{2m}}} \right] \times \left[\left(\frac{\theta_p}{1 - \theta_p} \right)^2 + \frac{\theta}{1 - \theta} \right]^{\frac{1-m}{2m}} \left(\frac{|\sigma_{zz}|}{A} \right)^{\frac{1}{m}} \quad (29)$$

Combining Eqs. (7) and (29) gives the following expressions for the rate-of-change of porosity:

$$\dot{\theta} = - \left(\frac{3}{2} \right)^{\frac{m-1}{2m}} \left[\frac{1 - \theta_p}{(1 - \theta)^{\frac{m+3}{2}}} \right]^{\frac{1}{m}} \left[\left(\frac{\theta_p}{1 - \theta_p} \right)^2 + \frac{\theta}{1 - \theta} \right]^{\frac{1-m}{2m}} \theta \left(\frac{|\sigma_{zz}|}{A} \right)^{\frac{1}{m}} \quad (30)$$

Combining Eqs. (7), (9) and (23) gives the following expression for the axial strain rate in terms of the rate-of-change of porosity:

$$\dot{\epsilon}_{zz} = \frac{\dot{H}}{H} = \frac{1}{3} \left[\frac{2\theta_p + \theta(1 - 3\theta_p)}{(1 - \theta_p)(1 - \theta)} \right] \frac{\dot{\theta}}{\theta} \quad (31)$$

Combining Eqs. (9), (23) and (31) gives the following expression for the radial strain rate in terms of the rate-of-change of porosity:

$$\dot{\epsilon}_{rr} = \frac{\dot{R}}{R} = \frac{1}{3} \left[\frac{\theta - \theta_p}{(1 - \theta_p)(1 - \theta)} \right] \frac{\dot{\theta}}{\theta} \quad (32)$$

The shape change rate from Eq. (8) can be represented as follows:

$$\dot{\gamma} = 2\sqrt{6} \left| \frac{(1 - \theta)(1 - k)}{2(2 - 3\theta) - k(4 - 3\theta)} \right| |\dot{\epsilon}_{zz}| \quad (33)$$

or taking into account Eq. (29):

$$\dot{\gamma} / \left[\sqrt{2/3} (|\sigma_{z0}|/A)^{\frac{1}{m}} \right] = \frac{18\theta_p}{3\theta_p - 2} \left[\frac{\theta}{4(1 - \theta) \left(\theta - \frac{\theta_p}{3\theta_p - 2} \right)} \right]^{\frac{1}{m}} \times \left[\frac{2 - 3\theta_p}{6\sqrt{6} \sqrt{\theta_p^2(1 - \theta) + \theta(1 - \theta_p)^2}} \right]^{\frac{m-1}{m}} \quad (34)$$

The normalized shape change rate $\dot{\gamma} / \left[\sqrt{2/3} (|\sigma_{z0}|/A)^{\frac{1}{m}} \right]$ is shown in Fig. 4 as a function of the specimen's porosity θ for different m and θ_p .

Subtracting Eq. (32) from (31) and integrating gives the following expression for the aspect ratio H/R :

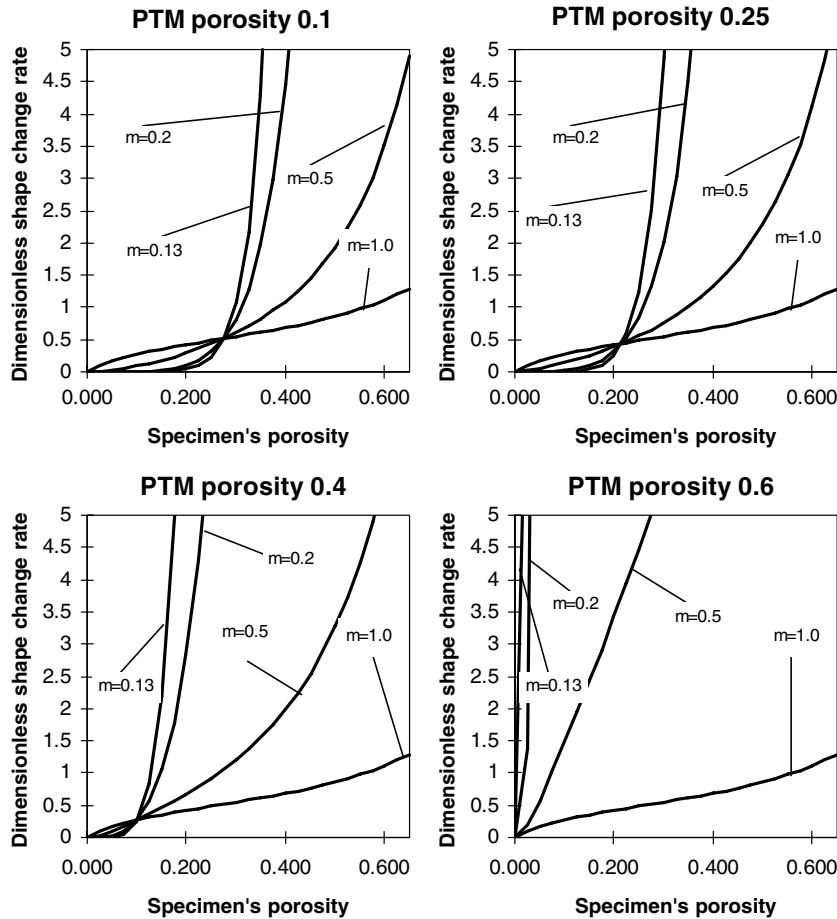


Fig. 4. Dimensionless normalized shape change rate vs. porosity for QIP.

$$\begin{aligned} \frac{\dot{H}}{H} - \frac{\dot{R}}{R} &= \left(\frac{\theta_p}{1 - \theta_p} \right) \frac{\dot{\theta}}{\theta} \Rightarrow \int_{\frac{H_0}{R_0}}^{\frac{H}{R}} d \left[\ln \left(\frac{H}{R} \right) \right] \\ &= \left(\frac{\theta_p}{1 - \theta_p} \right) \int_{\theta_0}^{\theta} d(\ln \theta) \Rightarrow \frac{H}{R} = \frac{H_0}{R_0} \left(\frac{\theta}{\theta_0} \right)^{\frac{\theta_p}{1 - \theta_p}} \end{aligned} \quad (35)$$

In deriving Eq. (35), it was assumed that θ_p is a constant (see Appendix). Eq. (35) indicates that the change in the aspect ratio H/R does not depend upon the constitutive behavior of either the PTM or densifying body, but depends only on the PTM's porosity and the body's initial density and dimensional parameters.

Eq. (35) can be compared with analogous expressions for conventional densification processes [28]:

$$\frac{H}{R} = \frac{H_0}{R_0} \left(\frac{\theta}{\theta_0} \right)^2 \quad \text{for free up-setting (pressing without lateral confinement, } \dot{\epsilon}_{rr} = 0) \quad (36)$$

$$\frac{H}{R} = \frac{H_0}{R_0} \left(\frac{1 - \theta_0}{1 - \theta} \right) \quad \text{for pressing in a rigid die (pressing with lateral confinement, } \dot{\epsilon}_{rr} = 0) \quad (37)$$

$$\frac{H}{R} = \frac{H_0}{R_0} \quad \text{for isostatic pressing (} \dot{\epsilon}_{rr} = \dot{\epsilon}_{zz} \Rightarrow \dot{\epsilon} = 3\dot{\epsilon}_{zz}; \dot{\gamma} = 0) \quad (38)$$

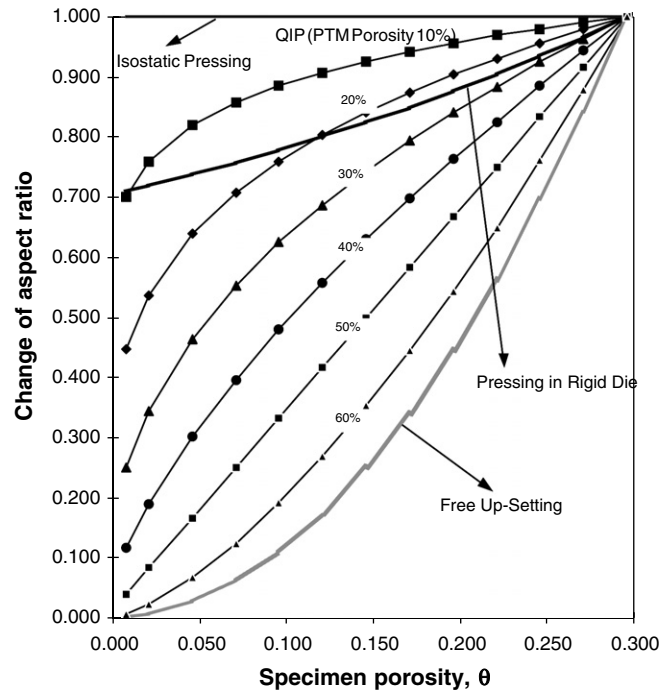


Fig. 5. Change of aspect ratio vs. porosity for different processes of treatment by pressure.

When $\theta_p = 2/3$, we obtain Eq. (36) derived for the conditions of free up-setting. If $\theta_p = 0$, we have the conditions of isostatic pressing (Eq. (38)) when $H/R = \text{const}$. If $\theta_p = \theta$ in the vicinity of $\theta = \theta_0$, we obtain Eq. (37), corresponding to the aspect ratio evolution in the conditions of pressing in a rigid die, as the first term of expansion of expression (35).

The results of the calculations in accordance with Eqs. (35)–(38) are shown in Fig. 5.

Change of the aspect ratio expressed by the relationship $\frac{H}{R} / \frac{H_0}{R_0}$ is represented as a function of the sample's porosity. The initial porosity of the sample is assumed to be $\theta_0 = 0.3$.

The calculation results indicate that, for sufficiently dense PTM, having porosity $\theta_p < 0.2$, the deformation state under QIP is close to the isostatic one. However, for most cases, in the capacity of PTM, industrial sand (alumina) mixed with graphite powder in a loose state is used.

For this PTM kind, $\theta_p > 0.2$. This means that the aspect ratio evolution under QIP can be close to that one obtained under the conditions of pressing in a rigid die or free up-setting.

4. Constitutive behavior of PTM

In order to understand the shrinkage and shape distortion of porous bodies densified in a granular PTM, it is important to understand the mechanical behavior of the PTM itself under compression load. The major question to be answered is the verification of the assumption made in Section 3. The model introduced in Section 3 assumed an elastic behavior of the PTM during compression. If this hypothesis is valid, then the dependence of the Young's modulus of the PTM with respect to the PTM

composition and the PTM porosity should obey certain rules. A series of experiments have been conducted to understand the evolution of the PTM Young's modulus during densification.

4.1. Experiments on PTM pressing in a rigid die

In our study, a mixture of 99% pure fused irregular shaped alumina (Al_2O_3) with typical size of 200 μm and 99% pure spherical shaped graphite (C) with typical size of 150 μm with different mass percentage was used as PTM. The alumina and graphite were mixed in a V-shape plastic container fixed in a rotary mixing machine for at least 8 h. The mixed PTMs were stored in sealed plastic containers for further use.

The PTM powders were placed in a rigid die with polished walls and with the inner diameter of 0.5 in. The PTM was pressed at a maximum load of 1.5 tons in an INSTRON™ machine, which recorded the load and the displacement. Thereby the stress–strain dependence during PTM compression has been determined for the composition range from 0% graphite and 100% alumina to 100% graphite and 0% alumina with an increasing (decreasing) step of 20% of each of the components. Based on these experimental data, one can obtain the evolution of the Young's modulus of the PTM powders during compression. At the same time, the relative density of the PTM powders during compression can be determined based on mass conservation. Fig. 6 shows a set of the normalized Young's modulus vs. relative density dependences for all the tested PTM compositions. (The Young's modulus for all the PTM compositions was normalized by the Young's modulus E_r (the reference Young's modulus) of the composition containing 50% Al_2O_3 and 50% C.)

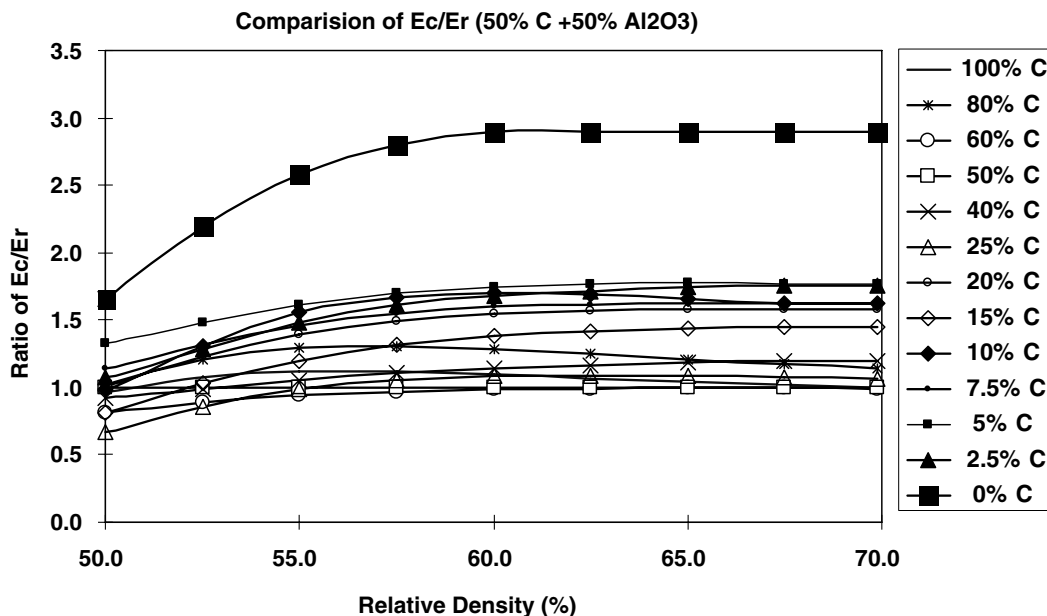


Fig. 6. Normalized Young's modulus vs. PTM relative density (the reference modulus is obtained for a fixed PTM composition).

The first set of tests indicated that there is a substantial change in the densification behavior when the composition of alumina is greater than 80%. Therefore, the additional tests with graphite composition of 25%, 15%, 10%, 7.5%, 5% and 2.5% were conducted.

The qualitative analysis of the PTM particles' response to the applied pressing load was carried out by scanning electron microscopy (SEM). The results of the scanning electron microscopy analysis of the loose PTM powder are shown in Fig. 7. It is evident (Fig. 7a and b) that graphite particles experience extensive damage at the first several cycles of the PTM usage (when "fresh" PTM is employed). Alumina particles, on the contrary, do not indicate any substantial evidence of cracking (Fig. 7a and c). In order to assess the degree of the deformation of the PTM during quasi-isostatic pressing, the recycled PTM alumina powder has been pressed with a polymeric binder (polychlorvinile) in a rigid die under 100 MPa pressure. The pressed specimens were removed from the die and polished using standard metallographic techniques. Examination of both the loose PTM powder and the pressed specimens was conducted using a Cambridge Stereoscan 360 SEM. The results of the SEM analysis of the pressed specimen are shown in Fig. 8.

No particle distortions or areas of a remarkable plastic flow are observed in Fig. 8. The results shown in Figs. 7c and 8 confirm an accepted hypothesis of a pure elastic deformation of the recycled PTM powder. The applicability of an elastic model for the description of the "fresh" PTM constitutive behavior is studied by the following quantitative analysis of the obtained experimental data on the PTM pressing in a rigid die.

4.2. Analysis of the experimental data

Fig. 5 indicates that the PTM's normalized Young's modulus (obtained as a slope on the corresponding stress–strain diagrams assuming the boundary conditions of the deformation in a rigid die), does not experience a substantial change when the relative density is greater than 60%. Therefore, it is appropriate to make an assumption that the PTM Young's modulus $E(C, \rho_p)$, which, in general, is a function of the PTM composition C and the PTM relative density ρ_p , can be represented as a product of two functions $E_c(C)$ and $E_{\rho_p}(\rho)$, where $E_c(C)$ is a function of the PTM composition C only and $E_{\rho_p}(\rho)$ is a function of the PTM relative density ρ only. (Indeed, this functional form justifies the independence of the concentration-normalized PTM Young's modulus of the PTM relative density.)

According to our assumption, we have:

$$E(C, \rho) = E_c \cdot E_{\rho_p} \quad (39)$$

Since E_c does not depend on the PTM relative density, we can use the effective Young's modulus for a fully dense PTM material for the purpose of finding a general expression of E_{ρ_p} as a function of the relative density ρ_p . From Eq. (39) we have:

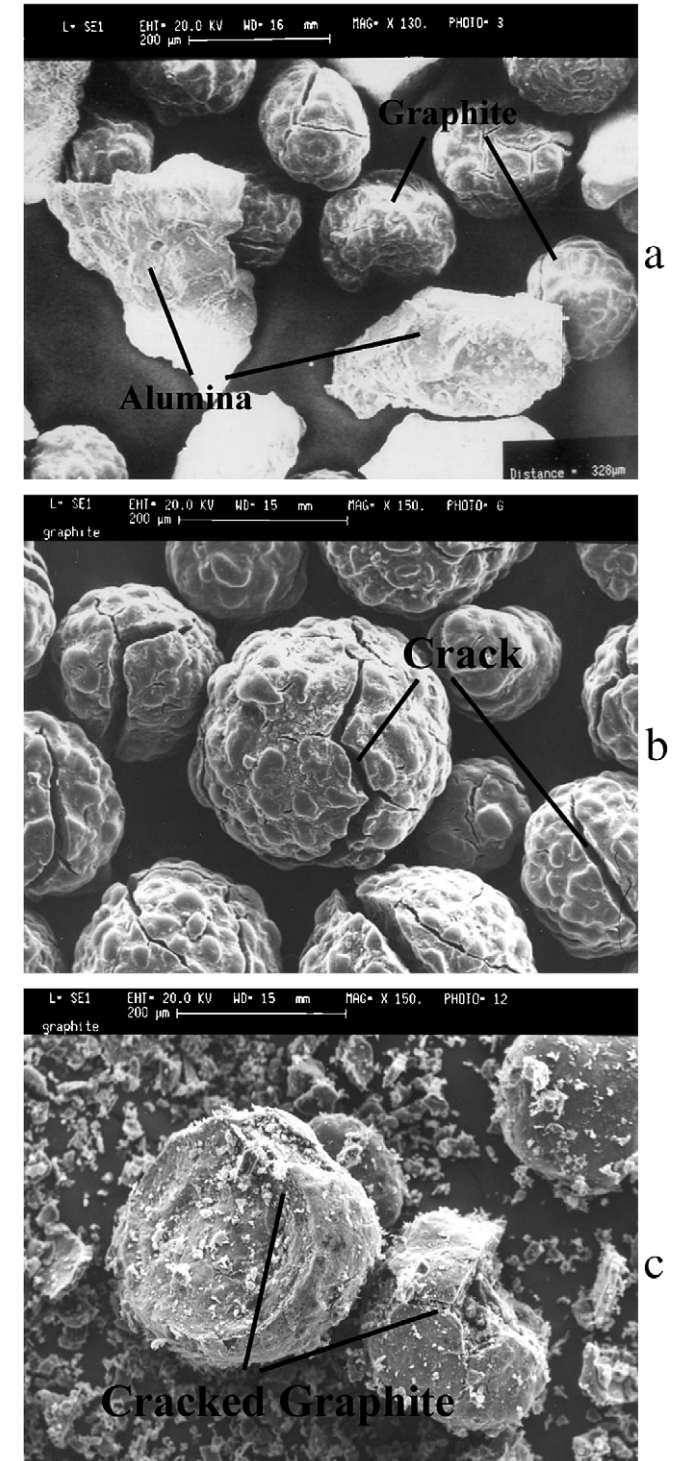


Fig. 7. SEM micrograph of the loose PTM powder: (a) 50% alumina and 50% graphite; (b) cracks on surfaces of graphite particles; (c) graphite particles after compression.

$$E_{\rho_p} = E(C, \rho_p) / E_c \text{ (Fully Dense)} \quad (40)$$

Here E_c (Fully Dense) is determined as a linear combination of the corresponding elastic moduli for alumina and graphite.

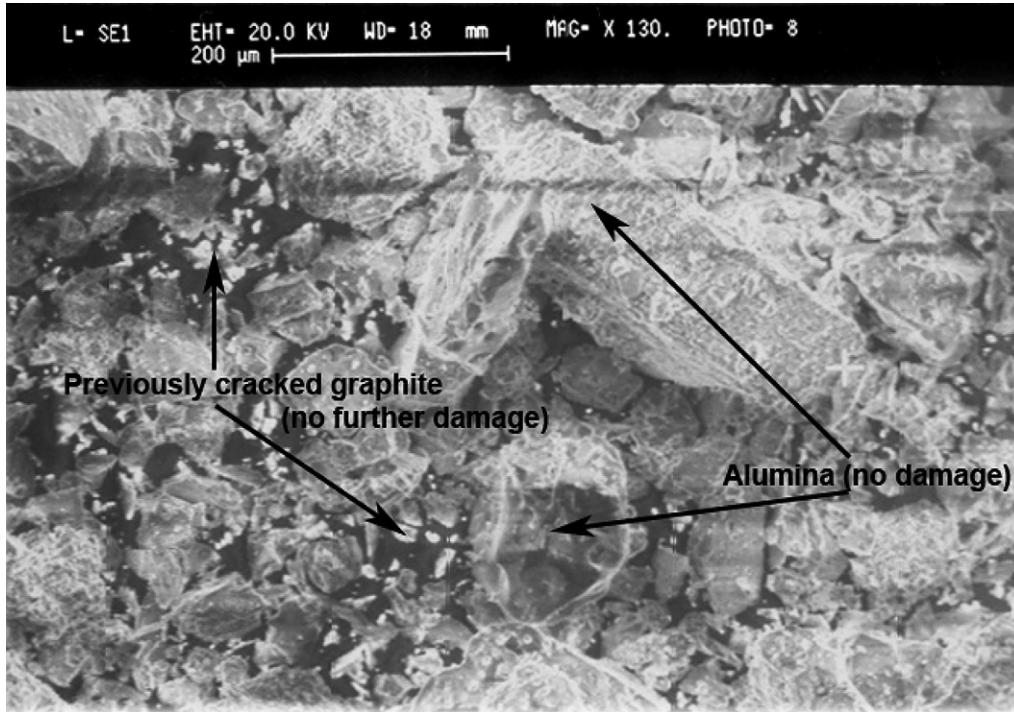


Fig. 8. SEM micrograph of the recycled alumina PTM powder pressed under 100 MPa with a polymeric binder in a rigid die.

Fig. 9 shows the experimental results for E_{ρ_p} for different PTM compositions. From this figure one can see that the obtained curves are very close to each other. This, in turn, indicates that E_{ρ_p} does not depend considerably on the PTM composition. This fact agrees with the above-mentioned assumption.

By taking a linear approximation of the average of all the curves in Fig. 9, a general expression for E_{ρ} can be determined:

$$E_{\rho_p} = 0.0188 \cdot \rho_p - 0.8764 \quad (41)$$

Following a similar process, from Eq. (39) we have:

$$E_C = E(C, \rho_p) / E_{\rho_p} \quad (42)$$

From Fig. 6, it follows that E_c/E_r does not change substantially for relative densities greater than 60%. This allows an approximation (as shown in Fig. 10) for E_c as:

$$E_c = 384.55 \cdot (C + 1)^{-0.22475} \quad (43)$$

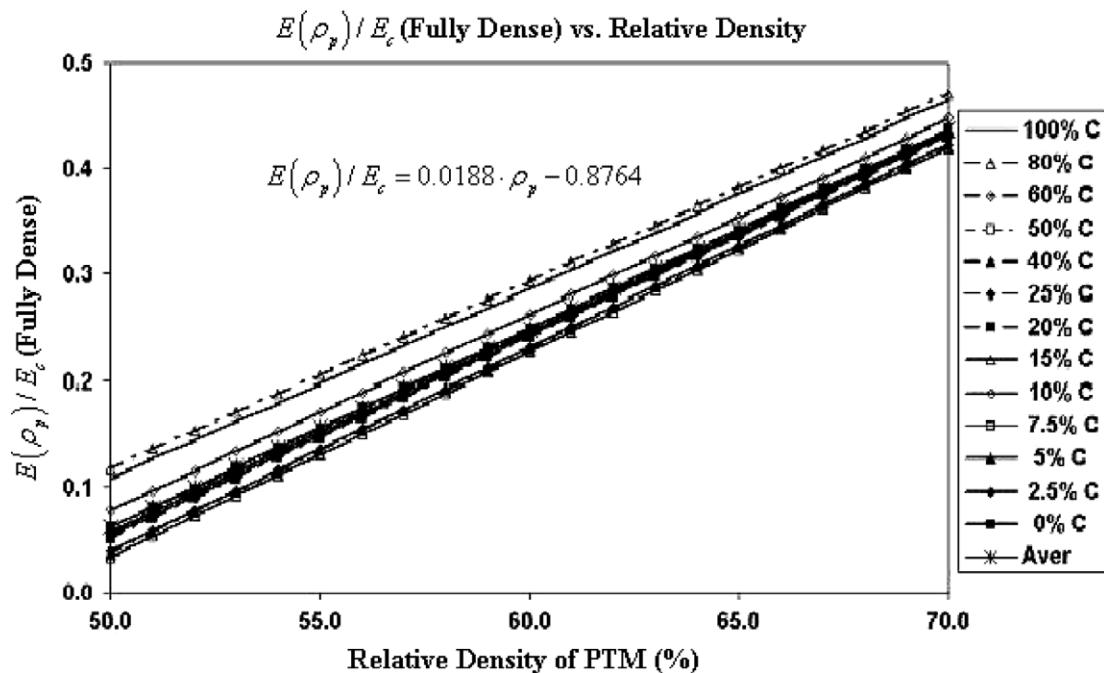


Fig. 9. Normalized Young's modulus vs. PTM relative density (the reference modulus is obtained for a fully dense PTM).

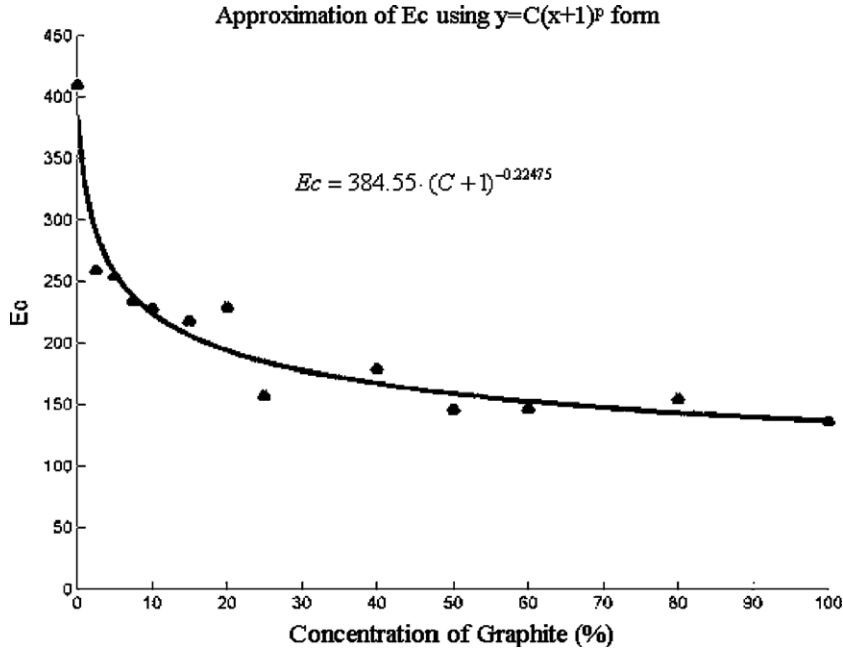


Fig. 10. Approximation of the concentration dependence of the PTM Young's modulus.

Combining Eqs. (41) and (43), we obtain the general expression for the PTM Young's modulus as a function of the PTM composition and the PTM relative density (used earlier as Eq. (20)):

$$E(C, \rho) = 384.55 \cdot (C + 1)^{-0.22475} (0.0188 \cdot \rho_p - 0.8764) \quad (44)$$

where C is the mass percentage of graphite in PTM and ρ_p is the PTM relative density during the compression process.

5. Optimization of PTM composition

Having determined the functional form of the elastic modulus, one can consider the influence of the PTM composition on the distortion of a porous body subjected to QIP. The elastic behavior of the PTM is determined by Hook's law. Therefore, the axial stress in the PTM can be represented as:

$$\sigma_{zp} = \frac{E}{1 + \nu} \left[\varepsilon_{zz} + \frac{\nu}{1 - 2\nu} (\varepsilon_{zz} + 2\varepsilon_{rr}) \right] \quad (45)$$

where E and ν are the PTM's Young's modulus and Poisson's ratio, respectively; ε_{zz} and ε_{rr} are the PTM axial and radial deformations, respectively. For a rigid die, $\varepsilon_{rr} = 0$, therefore:

$$\sigma_{zp} = \frac{E(1 - \nu)}{(1 - 2\nu)(1 + \nu)} \varepsilon_{zz} \quad (46)$$

The Poisson's ratio for a compressible PTM is accepted as [29]:

$$\nu = \frac{2 - 3\theta_p}{4 - 3\theta_p} \quad (47)$$

where $\theta_p = 1 - \rho_p$ is the relative porosity of the PTMs. From Eqs. (6) and (9), Eq. (8) can be written as:

$$\sigma_{zp} = 384.55(C + 1)^{-0.22475} (0.0188(1 - \theta_p) - 0.8764) \times \frac{1}{9} \frac{(4 - 3\theta_p)}{\theta_p(1 - \theta_p)} \varepsilon_{zz} \quad (48)$$

In Section 3, for the engineering assessment of the shape change during QIP (see Eq. (35)), the constancy of the PTM porosity θ_p has been assumed. Here, for the rigorous optimization analysis, we consider a more general case of evolving θ_p . Both solutions (with constant and changeable PTM porosity) are compared with the experimental data on cold and hot QIPing of cylindrical specimens in Section 7.

Substituting the expression for the axial strain (based on mass conservation),

$$\varepsilon_{zz} = \ln \frac{1 - \theta_{p0}}{1 - \theta_p} \quad (49)$$

where θ_{p0} is the initial PTM porosity, we obtain:

$$\sigma_{zp} = 384.55 \cdot (C + 1)^{-0.22475} (0.0188 \cdot (1 - \theta_p) - 0.8764) \times \frac{1}{9} \frac{(4 - 3\theta_p)}{\theta_p(1 - \theta_p)} \ln \frac{1 - \theta_{p0}}{1 - \theta_p} \quad (50)$$

Based on the analysis of the evolution of the PTM porosity (see Eq. (A4) in Appendix):

$$\sigma_{zz} = -\frac{2}{3} A |\dot{\varepsilon}|^m \frac{2 - 3\theta_p}{2 - \theta_p} \frac{(1 - \theta)^3}{\theta} \times \left[\frac{\sqrt{6}(1 - \theta) \sqrt{\theta_p^2(1 - \theta) + \theta(1 - \theta_p)^2}}{(4 - 3\theta_p)\theta} \right]^{m-1} \quad (51)$$

where parameters A and m are material constants. From our former study [30] on the testing by indentation of combustion synthesized cermet specimens, the values of $A = 180 \text{ MPa}^{0.2}$ and $m = 0.2$ were used in this work (these values were obtained for a TiC–NiTi cermet composite with the 30 vol.% NiTi). Equilibrium in the system PTM–specimen requires:

$$\sigma_{zp} = \sigma_{zz} \quad (52)$$

For the purpose of the generalization of the optimization results, a normalized time of $\tau = \left(\frac{A}{E_0}\right)^{\frac{1}{m}} t$ is introduced, where E_0 is the effective Young's modulus for a fully dense PTM material and t is the physical time of the process. Therefore, from Eqs. (12)–(14), we obtain:

$$\begin{aligned} \frac{d\theta}{d\tau} = & -(1-\theta) \left[\frac{576.83}{E_0} (C+1)^{(-0.22475)} (0.0188(1-\theta_p) - 0.8764) \right]^{\frac{1}{m}} \\ & \times \left[\frac{(4-3\theta_p)}{9\theta_p(1-\theta_p)} \ln \left(\frac{1-\theta_p}{1-\theta_{p0}} \right) \frac{(2-\theta_p)}{(2-3\theta_p)} \frac{\theta}{(1-\theta)^3} \right]^{\frac{1}{m}} \\ & \times \left[\frac{\sqrt{6}(1-\theta) \sqrt{\theta_p^2(1-\theta) + \theta(1-\theta_p)^2}}{\theta(4-3\theta_p)} \right]^{\frac{1-m}{m}} \end{aligned} \quad (53)$$

Here θ is the specimen's porosity.

$$\dot{\theta}_p = \frac{\left\{ \rho_{\text{Spe}} \left[2R\dot{R}H(1-\theta) + R^2\dot{H}(1-\theta) - R^2H\dot{\theta} \right] - \rho_{\text{PTM}} \left(R_d^0 \dot{\theta} + 2R\dot{R}H + R^2\dot{H} \right) (1-\theta_p) \right\}}{\rho_{\text{PTM}} \left[R_d^0 (H_d^0 - \dot{\theta}t) - R^2H \right]} \quad (58)$$

Based on Eqs. (8), (10) and (23), the following kinetic differential equations are valid for the normalized dimensions H/H_0 and R/R_0 , where H and H_0 are the current and the original heights of the specimen, respectively, and

$$\frac{d(\theta_p/\theta_{p0})}{d\tau} = \frac{\left\{ \frac{\rho_{\text{Spe}}}{\rho_{\text{PTM}}} \left(2 \frac{R}{R_0} \frac{H}{H_0} \frac{d(R/R_0)}{d\tau} (1-\theta) + \left(\frac{R}{R_0} \right)^2 \frac{d(H/H_0)}{d\tau} (1-\theta) - \left(\frac{R}{R_0} \right)^2 \frac{H}{H_0} \frac{d\theta}{d\tau} \right) - \left[\left(\frac{R_d^0}{R_0} \right)^2 \frac{\dot{\theta}}{H_0} \left(\frac{A}{E_0} \right)^{\frac{1}{m}} + 2 \frac{R}{R_0} \frac{H}{H_0} \frac{d(R/R_0)}{d\tau} + \left(\frac{R}{R_0} \right)^2 \frac{d(H/H_0)}{d\tau} \right] (1-\theta_p) \right\}}{\left[\left(\frac{R_d^0}{R_0} \right)^2 \left(\frac{H_d^0 - \dot{\theta}(A/E_0)^{\frac{1}{m}} \tau}{H_0} \right) - \left(\frac{R}{R_0} \right)^2 \frac{H}{H_0} \right]} \quad (59)$$

R and R_0 are the current and the initial radii of the specimen, respectively:

$$\frac{d(H/H_0)}{d\tau} = \frac{H}{3H_0} \left[\frac{2\theta_p + (1-3\theta_p)\theta}{\theta(1-\theta)(1-\theta_p)} \right] \frac{d\theta}{d\tau} \quad (54)$$

$$\frac{d(R/R_0)}{d\tau} = \frac{R}{3R_0} \left[\frac{\theta - \theta_p}{\theta(1-\theta)(1-\theta_p)} \right] \frac{d\theta}{d\tau} \quad (55)$$

Based on the mass conservation of the whole system, including both a PTM and a porous cylindrical specimen, the following is correct:

$$\frac{dM}{dt} = \rho_{\text{Spe}} \frac{dV_{\text{Spe}}}{dt} + \rho_{\text{PTM}} \frac{dV_{\text{PTM}}}{dt} = 0 \quad (56)$$

where ρ_{Spe} is the density of the fully dense specimen, V_{Spe} is the skeleton volume (substance volume excluding the volume of pores) of the specimen, ρ_{PTM} is the density of the

fully dense PTM and V_{PTM} is the skeleton volume of the PTM.

The following geometric relationships are valid:

$$\begin{aligned} V_{\text{Spe}} &= \pi R^2 H (1-\theta) \\ V_{\text{PTM}} &= \pi (R_d^0 H_d - R^2 H) (1-\theta_p) \end{aligned} \quad (57)$$

where R_d^0 is the radius of the rigid die used to contain the whole composite cell (composite cell includes both PTM and densified specimen) and H_d is the current height of the whole composite cell, which is equal to $H_d^0 - \dot{\theta}t$ (H_d^0 is the initial height of the composite cell and $\dot{\theta}$ is the speed of punch).

Substituting Eq. (57) into (56) and simplifying the results, we have:

Applying the same normalization procedures as used before in Eq. (53) for the time t , the specimen height H , the specimen radius R and the PTM porosity θ_p , Eq. (58) can be rewritten as:

Eqs. (53)–(55) and (59) represent a set of four first-order differential equations with respect to the four unknown functions of the specific time τ : specimen's porosity θ , specimen's height H , specimen's radius R and the PTM porosity θ_p . Fig. 11 shows the solution of the above-mentioned set of equations (using the fourth-order Runge–Kutta algorithm). This solution has been obtained for the PTM with alumina concentration of 50%. Similar solutions were obtained for various compositions of the PTM. All of them indicate almost no porosity and distortion level change for the time range exceeding 12 s. The shrinkage and distortion rates for this time point are comparatively assessed in Fig. 12. This figure shows the rate of the distortion $\left(\frac{d((H/H_0)/(R/R_0))}{dt}\right)$ and the densification $(d\theta/dt)$ rate for different PTM compositions. From this figure one can see that at the composition of 75% Al_2O_3 and 25% C the curve of densification rate crosses the curve of the distortion rate. This point corresponds to the highest densification rate while

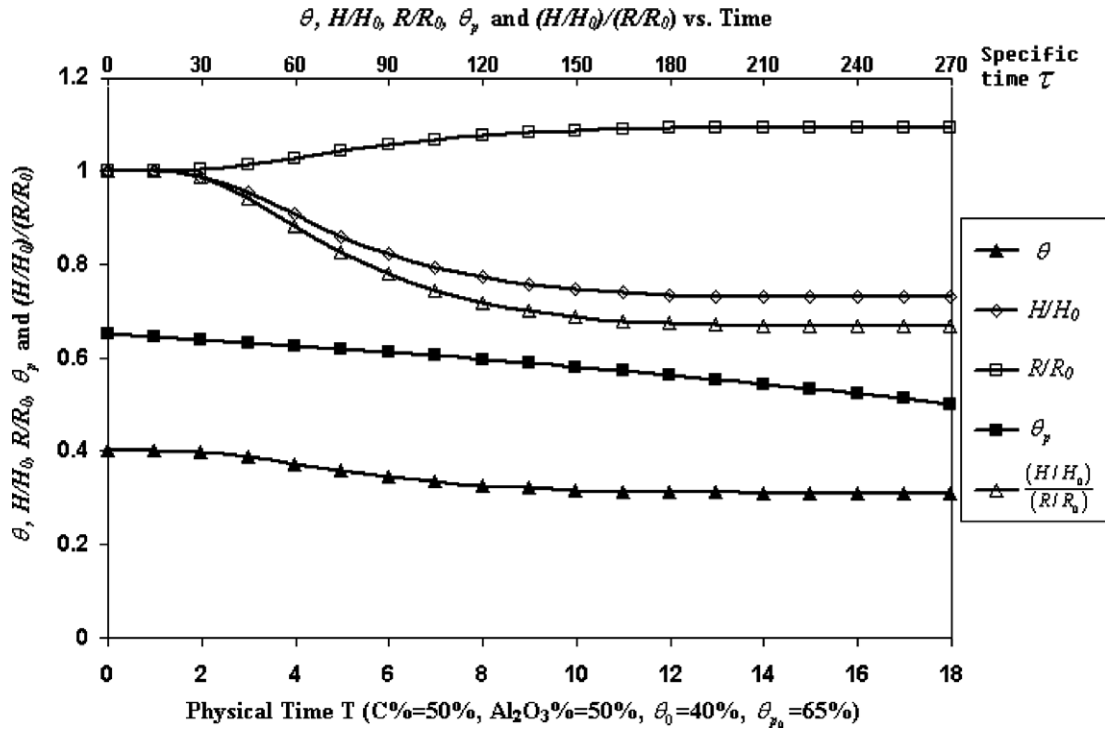


Fig. 11. Kinetics of shrinkage and distortion.

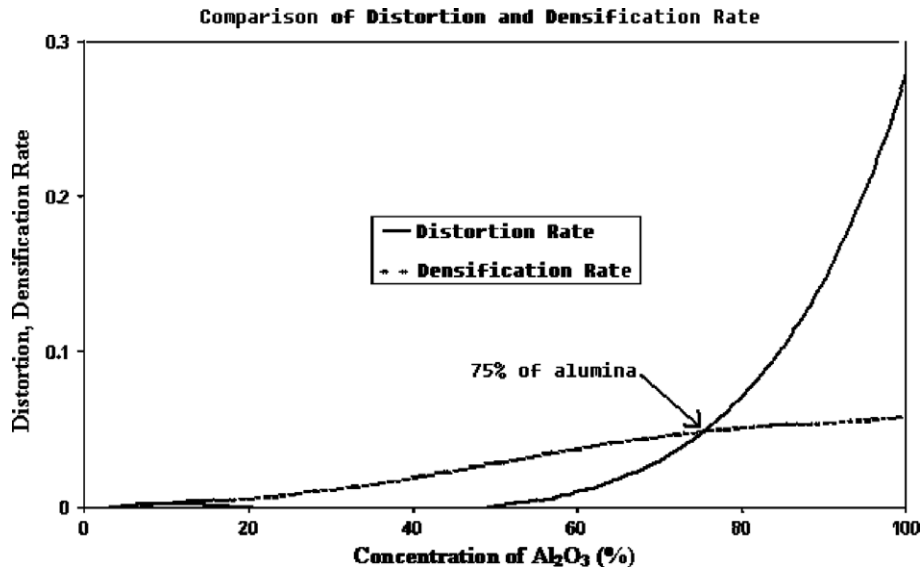


Fig. 12. Comparative analysis of densification and distortion rates.

the distortion rate is at its lowest possible level. Therefore, for the chosen values of the specimen’s constitutive parameters (constants A and m), the PTM composition containing 75% of alumina and 25% of graphite should be optimal.

6. QIP experiments

6.1. Cold QIP experiments

For the analysis of the aspect ratio evolution and the verification of the modeling results obtained in previous

sections, quasi-isostatic pressing of Ni and Ti powder samples was carried out in a rigid cylindrical die at room temperature. A graphite powder transmitting medium was used in the experiments. The velocity of pressing was approximately 0.001 m/s. The die dimensions were 0.06 m diameter and 0.1 m height.

The die was designed to withstand 200 MPa of internal pressures. A smaller, thinner can (approximately 1 mm) was encased in a structural thick wall cylinder. The piston maintained pressure with a hardened steel seal plate.

Table 1
Comparison of the theoretical and experimental results on QIPing of Ni and Ti porous samples

	Initial height (m)	Initial diameter (m)	Final height (m)	Final diameter (m)	Initial porosity	Final porosity	Change of aspect ratio (experimental)	Change of aspect ratio (theoretical)	Relative error
Nickel	0.030	0.032	0.026	0.032	0.47	0.388	0.871	0.881	0.011
Nickel	0.012	0.032	0.01	0.032	0.48	0.346	0.814	0.804	0.013
Nickel	0.016	0.032	0.011	0.032	0.51	0.278	0.713	0.667	0.065
Titanium	0.025	0.032	0.022	0.032	0.52	0.461	0.889	0.923	0.039
Titanium	0.038	0.032	0.031	0.032	0.5	0.374	0.813	0.823	0.012
Titanium	0.025	0.032	0.021	0.032	0.45	0.344	0.841	0.836	0.005

Nickel and titanium specimens were produced by the preliminary cold pressing of loose powders. The cold pressing was performed to produce three nickel and three titanium samples, the heights and diameters of which are given in Table 1.

Each cold pressed sample was heated in a furnace to lower its yield stress and to improve the integrity of the samples by providing some degree of sintering; the nickel samples were heated to 615 °C and the titanium samples to 350 °C. Without pre-sintering of the samples, they could potentially have been crushed during the QIP process. Upon removal from the furnace each sample was immediately placed in a thin-walled can (6 in diameter) and surrounded by the PTM. The can was introduced inside a thick-walled pressure cylinder and the piston with the plunger assembly was placed on the top of the PTM. The samples were then pressed to a variety of forces, ranging from 2.5 to 10 kN.

The diameter, the height and the porosity of all the samples were measured before and after QIP. The porosity measurements were performed by the method of optical metallography. The results of experiments are represented in Table 1.

6.2. Hot QIP experiments

The hot QIP was conducted at the post-combustion (SHS) densification stage employed for the synthesis of TiC–TiNi cermet composites (for more details, see our previous publications [13,15]). The first step was baking of the elemental titanium, nickel and graphite powders (with 30 vol.% of TiNi – 0.76 mol fraction of TiC). The elemental powders were baked under a temperature of 110 °C and under a less than 25 mm Hg pressure in a vacuumed oven for at least 24 h. The baked powders were loaded under argon protection into polyethylene

jars and dry mixed with corundum grinding balls (96.3% Al₂O₃ and 2.75% SiO₂) in a grinding ball/powder mass ratio of 4:1. Thereafter, the polyethylene jars were fixed onto a rotary blender machine and dry mixed for at least 24 h. After mixing, the mixture was put back into the vacuum oven and again baked for at least another 24 h under 110 °C and less than 25 mm Hg pressure to remove the moisture absorbed in the mixture. After baking, mixtures of the powders were uniaxially pressed into cylindrical specimens with dimension of approximately either diameter 1.25 in. and height 0.6 in. (weight approximately 25 g) or diameter 1.25 in. and height 1.25 in. (weight approximately 50 g) under a compressing load of 2 tons in a rigid die. Right after the green sample was ready it was loaded into the center of a pool of PTM (of the optimal composition determined in Section 5 – 75% Al₂O₃ and 25% C) in a 6-inch-diameter die. Thereafter, it was ignited and sequentially consolidated using PHI and ENERPAC presses.

To aid the initiation of the combustion and thereafter a planar combustion wave from the top of the specimen, samples were placed beneath a layer of loose stoichiometric titanium–graphite mixture. An electrochemical system consisting of a resistant Ni–Cr heating wire was wrapped around a wooden matchstick and buried in the loose powder. A remote variable transformer was connected to the resistant heating wire and the combustion was initiated by passing an electrical current through the resistant heating wire and consecutive ignition of the matchstick. Following the combustion synthesis, after a time delay of 15 s, a load of 10 kN have been applied for 20 s. Fig. 14 compares the microstructure of the as-reacted material (Fig. 14a) to the same material loaded to 10 kN after a delay time of 15 s (Fig. 14b). The final porosity is in the range of 1–3%.

Table 2
Comparison of the theoretical and experimental results on QIPing of TiC–TiNi powder cermet composites

TiC–30 vol.%TiNi	Initial height (m)	Initial diameter (m)	Final height (m)	Final diameter (m)	Initial porosity	Final porosity	Change of aspect ratio (experimental)	Change of aspect ratio (theoretical)	Relative error
1	0.0320	0.0320	0.0150	0.0388	0.335	0.032	0.385	0.365	0.054
2	0.0150	0.0320	0.0072	0.0380	0.350	0.033	0.401	0.363	0.095

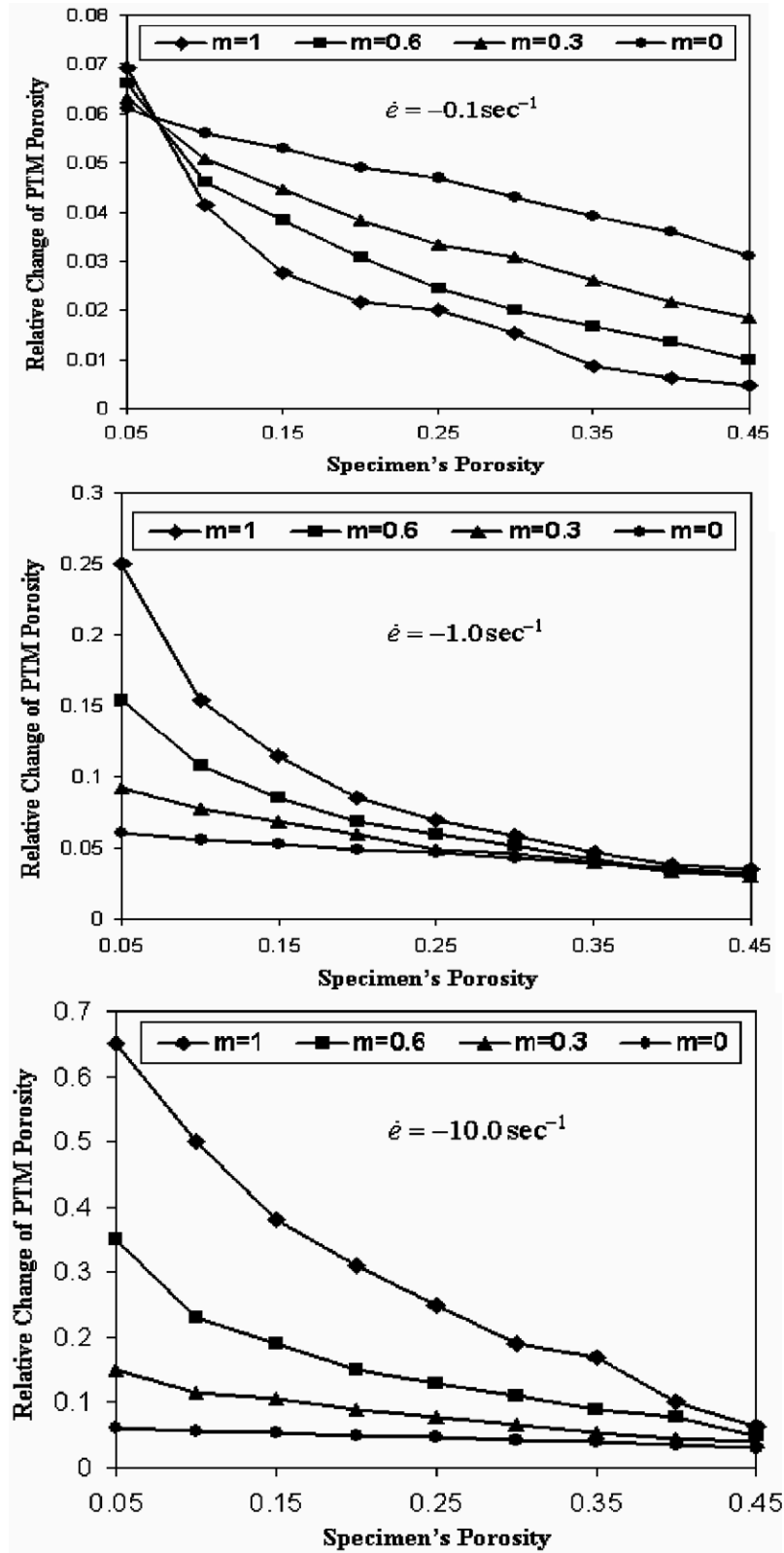


Fig. 13. Relative change of the PTM porosity $\frac{\theta_p - \theta_{p0}}{\theta_{p0}}$ vs. sample porosity for different sample skeleton strain rate sensitivities (m) and process rates ($\dot{\epsilon}$).

The diameter, the height and the porosity of all the samples were measured before and after combustion following QIP. The porosity measurements

were performed using the Archimedes technique [1]. The results of experiments are represented in Table 2.

7. Comparison of modeling and experimental data

Based on the experimental data on initial parameters (aspect ratio and porosity) for QIP of Ni and Ti powder samples, the calculations were performed in conformity to Eq. (35). The final aspect ratio was determined with the knowledge of the sample final porosity. PTM (graphite powder) porosity was determined experimentally (using mass conservation-based calculations): $\theta_p = 0.4$. This value was used in the analysis.

The experimental and theoretical data are given in Table 1. One can see that the experimental and calculated results agree well: for all the cases, the relative error in the values of the final aspect ratio is less than 6.5%. Thus, Eq. (35) can be recommended for use as a practical tool for the quantitative prediction of the shape change during (cold) QIP.

It should be noted that Eq. (35) is not valid for a fast pressing accompanied by high-strain-rate modes (faster than 1 s^{-1} ; see Fig. 13). In this case, Eq. (35) in its differential form should be solved with regard to Eq. (A6) (see Appendix).

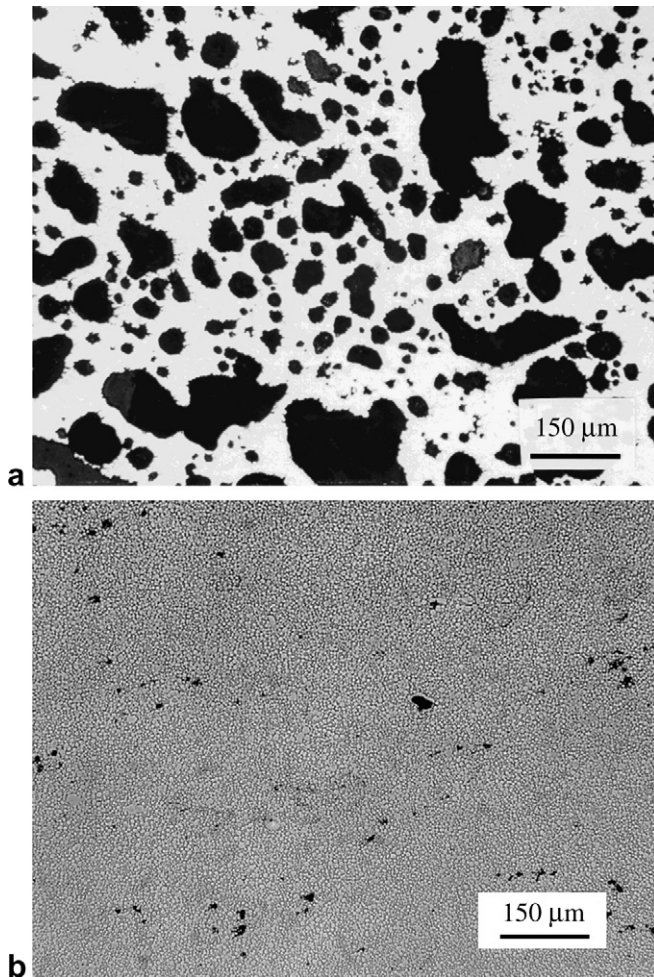


Fig. 14. Microstructures of (a) the as-reacted and (b) the densified (subjected to QIP) TiC-TiNi cermet.

The comparison of the experimental data on the shape evolution during hot QIPing of combustion-synthesized TiC-TiNi cermet composites with model predictions provided by the solution of Eqs. ((53)–(55) and (59)) is given in Table 2 for both size sets of specimens mentioned in Section 6. The initial PTM porosity assumed was $\theta_p = 50\%$. One can see that the relative error in the values of the final aspect ratio is smaller than 10% (see Table 2).

8. Conclusions

The principal results obtained in the investigation can be summarized as follows:

1. A mathematical model of the quasi-isostatic pressing (QIP) is developed.
2. The model predicts an essential shape change under QIP for large porosities of the pressure-transmitting medium (PTM).
3. It is shown that, for most cases, the QIP deformation mode has an intermediate position between the deformation modes of pressing in rigid dies and free upsetting.
4. The ratio between the sample and the PTM porosities influences the evolution of the integral aspect ratio.
5. The assumption of the elastic character of the PTM constitutive behavior is analyzed. The dependence of the PTM elastic modulus on the PTM composition and the PTM relative density is determined.
6. An algorithm for the determination of the optimal PTM composition is developed. The algorithm is aimed at finding the PTM composition that enables the highest densification of the porous specimen with the minimum possible distortion. It is shown that, for TiC-TiNi cermet composites, the optimal PTM composition corresponds to 75 mass% alumina and 25% graphite.
7. A comparison of the experimental and calculation results on cold QIPing of Ni and Ti powders and hot QIPing of TiC-TiNi cermet composites demonstrates good quantitative correspondence.

Acknowledgement

This work was partially supported by the NSF Division of Manufacturing and Industrial Innovation, Grant DMI-0354857.

Appendix. Evolution of PTM porosity during QIP

In the following, E and ν are the PTM Young's modulus and Poisson's ratio, respectively; ϵ_{zz} and ϵ_{rr} are the PTM axial and radial deformations, respectively.

The following expressions for E and ν are valid (by analogy "linear viscosity = elasticity": $\eta_0 \leftrightarrow \frac{E_0}{2(1+\nu_0)}$ for fully dense material, $\eta_0 \phi \leftrightarrow \frac{E}{2(1+\nu)}$ for effective porous material; $\nu_0 = \frac{1}{2}$ for an incompressible skeleton):

$$E = 4E_0 \frac{(1 - \theta_p)^2}{4 - 3\theta_p}, \quad \nu = \frac{2 - 3\theta_p}{4 - 3\theta_p} \quad (\text{A1})$$

Then, Eq. (46) can be rewritten as:

$$\sigma_{zp} = \frac{4}{9} E_0 \frac{(1 - \theta_p)^2}{\theta_p} \varepsilon_{zz} \quad (\text{A2})$$

Expression (A2) reflects the fact that an infinite stress is necessary for bringing a body into the poreless (fully dense) state.

Substituting Eq. (49) for the axial strain (based on mass conservation), we obtain:

$$\sigma_{zp} = \frac{4}{9} E_0 \frac{(1 - \theta_p)^2}{\theta_p} \ln \frac{1 - \theta_p}{1 - \theta_p} \quad (\text{A3})$$

At the same time, for the sample, Eqs. (7) and (28) are valid. Upon their basis, we have the relationship for the axial stress in the sample:

$$\sigma_{zz} = -\frac{2}{3} A |\dot{\varepsilon}|^m \frac{2 - 3\theta_p}{2 - \theta_p} \times \frac{(1 - \theta)^3}{\theta} \left[\frac{\sqrt{6}(1 - \theta) \sqrt{\theta_p^2(1 - \theta) + \theta(1 - \theta_p)^2}}{(4 - 3\theta_p)\theta} \right]^{n-1} \quad (\text{A4})$$

Equilibrium in the system PTM–sample requires:

$$\sigma_{zp} = \sigma_{zz} \quad (\text{A5})$$

Thus, from Eqs. (A3)–(A5) we obtain:

$$\frac{A |\dot{\varepsilon}|^m}{E_0} = \frac{2(1 - \theta_p)^2(2 - \theta_p)\theta}{3(2 - 3\theta_p)(1 - \theta)^3\theta_p} \times \ln \frac{1 - \theta_p}{1 - \theta_p} \left[\frac{\sqrt{6}(1 - \theta) \sqrt{\theta_p^2(1 - \theta) + \theta(1 - \theta_p)^2}}{(4 - 3\theta_p)\theta} \right]^{n-1} \quad (\text{A6})$$

The latter expression enables the analysis of the relative change of the PTM porosity $\frac{\theta_{p0} - \theta_p}{\theta_{p0}}$ corresponding to definite values of the sample porosity, the strain rate sensitivity m and the volume change rate $\dot{\varepsilon}$. Note that, for most materials, $\frac{A}{E_0} \approx 10^{-3} \dots 10^{-2} s^m$ for the range of temperatures corresponding to hot deformation (A depends on the temperature) [27,31]

The results of the calculations in accordance with (A6) are represented in Fig. 13. Here, the initial PTM porosity θ_{p0} is assumed to be 0.65, and $\frac{A}{E_0}$ is taken $10^{-2} s^m$.

The calculation data indicate that, for higher strain rates, influence of the sample material strain rate sensitivity m on the change of the PTM porosity increases. For higher strain rates, the larger change of the PTM porosity occurs when the sample properties are close to the linear-viscous ones ($m \rightarrow 1$). For smaller strain rates (slower pressing),

the higher change of the PTM porosity corresponds to the ideal-plastic properties of the sample ($m = 0$).

The smaller the sample porosity, the higher the relative change of the PTM porosity.

For usual uniaxial pressing, strain rates vary in the range $10^{-3} \dots 10^{-2} s^{-1}$. As it follows from Fig. 13, for such a level of $\dot{\varepsilon}$, the relative change of the PTM porosity is always less than $\sim 6\%$. Therefore, for slow QIP processing, one can assume that the PTM porosity is unchangeable.

References

- [1] German RM. Powder metallurgy science. 2nd ed. Princeton, NJ: Metal Powder Industries Federation; 1994.
- [2] Raman RV, Rele SV, Poland S, LaSalvia J, Meyers MA, Niiler AR. J Metals 1995;3:23–5.
- [3] LaSalvia JC, Kim DK, Meyers MA. Mat Sci Eng 1996;A206:71–80.
- [4] Raman RV, Janney MA, Sastri SA. World congress on powder metallurgy. Washington, DC. Princeton, NJ: MPIF; 1996. p. 131.
- [5] Fu ZY, Wang WM, Yuan RZ, Munir ZA. Int. J. SHS 1993;2:307–13.
- [6] Ohyanagi M, Fukushima M, Koizumi M. In: Proceedings of the international conference on hot isostatic pressing, Andover, MA: 1996, p. 289–94.
- [7] Shingu PH, Ishihara KN, Ghonome F, Hyakawa T, Abe M, Tagushi K. In: Proceedings of the 1st US–Japan workshop on combustion synthesis (Tsukuba), 1990; p. 65–71.
- [8] Bogatov YV, Levashov E, Pityulin AN. Sov. Powder Metallurgy 1991;7(343):76–8.
- [9] Mihelic B, Dikic M, Djekic R, Uskokovic D. Mater Lett 1992;13:391–5.
- [10] LaSalvia JC, Meyers MA. Int J SHS 1995;4:43–57.
- [11] LaSalvia JC, Kim DK, Lipsett RA, Meyers MA. Met Mat Trans A 1995;26A:3001–9.
- [12] LaSalvia JC, Meyers MA. Met Mat Trans A 1995;26A:3011–9.
- [13] Olevsky EA, Kristofetz ER, Meyers MA. Int J SHS 1999;7(4):517–28.
- [14] Han JC, Zhang XH, Wood JV. Mater Sci Eng A 2000;280(2):328–33.
- [15] Olevsky EA, Strutt ER, Meyers MA. J Mater Proc Technol 2002;121(1):157–66.
- [16] Fedotov AF, Amosov AP. Powd Met Metal Ceram 2002;41(1–2).
- [17] Zhang WF, Zhang XH, Wang HL, Hong CQ. Mat Sci Eng A 2004;381(1–2):92–7.
- [18] Timokhova MI. Refract Indus Ceram 2004;45(5):320–3.
- [19] Pacheco MM, Stuiyinga M, Carton EP, Katgerman L. Mater Sci Forum 2005;492–493:63–8.
- [20] Burkes DE, Gottoli G, Yi HC, Moore JJ. Met Mat Trans 2006;37A(1):235–42.
- [21] Merzhanov AG, Borovinskaya IP. Doklady Akad Nauk SSSR 1972;204:366.
- [22] Olevsky EA, German RM. Acta Mater 2000;48:1153–66.
- [23] Olevsky EA, German RM. Acta Mater 2000;48:1167–80.
- [24] Olevsky EA, Molinari A. Int J Plasticity 2000;16:1–37.
- [25] Olevsky E. Mater Sci Eng R Rev 1998;23:41–100.
- [26] Olevsky E, Dudek HJ, Kaysser WA. Acta Met Mater 1996;44(2):707–13.
- [27] Ashby MF. HIP 6.0. Background reading. Cambridge: Engineering Department; 1990.
- [28] Olevsky E, Molinari A. Mech Mater 2006;38:340–66.
- [29] Skorohod VV. Rheological basis of the theory of sintering. Kiev: Naukova Dumka; 1972.
- [30] Olevsky EA, Strutt ER, Meyers MA. Scripta Mater 2001;44:1139–46.
- [31] Ashby MF, Jones DRH. Engineering materials 1. An introduction to their properties and applications. Int Series Mater Sci Technol 1987;34:31.